Environmental Fluid Mechanics (2025) 25:13
https://doi.org/10.1007/s10652-025-10017-5

ORIGINAL ARTICLE

Modeling of wind-driven circulation of schistosome larvae in a vegetated side pond

Brooke J. Pauken[1] · Andrew J. Chamberlin[2] · Chelsea L. Wood[3] · Oliver B. Fringer[1,2] · Giulio A. De Leo[2]

Received: 28 June 2024 / Accepted: 15 November 2024 / Published online: 18 February 2025

Abstract

Schistosomiasis, a debilitating parasitic disease of poverty affecting more than 250 million people worldwide, is contracted upon contact with the larval form of the parasite, known as cercaria, emerging from infected freshwater snails, the obligate intermediate host of the parasite. Understanding how infectious larvae can be transported in rivers and irrigation canals is crucial to fine-tune environmental interventions targeting the parasite and its intermediate host. Specifically, lateral cavities along many tropical rivers act as water access points but can also entrap parasitic larvae and provide low-velocity environments for snail-supporting vegetation to flourish, creating potential areas of high schistosomiasis infection. In this paper, the circulation of larvae in a typical transmission site along the Lampsar River in Senegal is modeled under a range of wind and vegetation conditions to better understand how such environmental factors affect their transport. We found that wind direction has a large influence on the distribution and abundance of parasitic larvae at the water access point, whereas increasing wind speed scales velocities but does not affect flow patterns. The area of coverage of vegetation can significantly alter flow magnitudes and circulation patterns for the same wind speed and direction. Increasing vegetation coverage generally leads to an increase in larvae residence time in the side pond, but the relationship is non-monotonic with five regimes of residence time behavior based on vegetation patch radius. The results suggest that there is an optimal patch radius at which larvae residence time and velocity deviations within the side pond are maximized.

Article Highlights

- Transport of schistosome larvae in a side pond along the Lampsar River is modeled under various vegetation and wind conditions

✉ Brooke J. Pauken
bpauken@stanford.edu

[1] Department of Civil and Environmental Engineering, Stanford University, Stanford, CA 94305, USA

[2] Oceans Department, Stanford University, Pacific Grove, CA 93950, USA

[3] School of Aquatic and Fishery Sciences, University of Washington, Seattle, WA 98195, USA

- Wind direction and vegetation area coverage have the largest impacts on flow patterns within the side pond
- Larvae residence times tend to increase with added vegetation but show varied behavior for ranges of vegetation patch radii

Keywords Particle tracking · Lateral cavity · Wind-driven flow · Schistosomiasis parasites

1 Introduction

Schistosomiasis is a parasitic disease of poverty, endemic in tropical and sub-tropical countries. Over 250 million individuals are treated for schistosomiasis every year, and 800 million are at risk of infection [1]. Schistosome parasites have a complex life cycle that includes freshwater snails as obligate intermediate host. Infected snails shed the free-living larval form of the parasite, called cercaria, that infects people when they step into parasite-contaminated waters for their daily chores [2]. Preventative treatment for schistosomiasis by the antihelminthic medication Praziquantel is effective at decreasing severity of symptoms and morbidity rates but does not prevent reinfection and requires several rounds of mass drug administration in the effort to extirpate the diseases from endemic regions [2]. Transmission interruption also requires environmental interventions that target the parasites when outside the human host by using molluscicide, through removal of aquatic vegetation, or by introducing natural predators [3–6].

Cercariae, the infectious larval stage of the parasite, are negatively buoyant and capable of swimming at speeds on the order of 0.1 to a few mm s^{-1}, generally alternating between free-sinking and active swimming [7]. Krishnamurthy et al. [7] estimated a Reynolds number of cercariae swimming $\mathrm{Re} = \langle V_{\mathrm{tail-first}} \rangle L/\nu \approx 0.3$, where $\langle V_{\mathrm{tail-first}} \rangle = 0.7$ mm s^{-1} is the mean tail-first swimming speed measured in their experiments, $L \approx 500$ μm is the cercaria length, and $\nu = 10^{-6}$ $m^2 s^{-1}$ is the kinematic viscosity of water. This Reynolds number quantifies the relative importance of inertial to viscous forces, with Re<1 indicating that inertial forces can be neglected in modeling cercariae swimming. This swimming can be stronger than vertical flow fluctuations, allowing cercariae to alter their position in the water column to seek hosts and in response to other environmental stimuli [8]. Their motility is largely limited to the vertical, as even weak environmental flows generally overpower their swimming capabilities in the horizontal. However, as flow speed varies with depth, cercariae can sample different velocities as they move up or down, potentially altering their dispersion [9]. The larvae have elongated approximately ellipsoidal bodies about 500 μm in length [7]. The movement of ellipsoidal particles in shear flows has been investigated in a number of studies, both experimentally [10, 11] and with models [12–14]. Ellipsoidal particles tend to preferentially align their primary axis with or against the mean direction of fluid motion, dependent on both their aspect ratio and the type of flow, although they may also oscillate about this preferential alignment. The orientation of an ellipsoid relative to the direction of flow can affect its drag force as well as its direction of travel [14].

On a larger scale, cercariae could theoretically disperse for tens to hundreds of meters from where they are released when transported by water [7]. Although seminal papers have been published to described disease dynamics of water associated on river networks (see for instance Ciddio et al. [15], Perez-Saex et al. [16] and [17], for schistosomiasis; Mari et al. [18] for cholera; Rinaldo et al. [19] for general disease networks), no published study

has so far investigated schistosome larvae transportation at this scale through the use of rigorous hydrodynamic circulation models. Understanding how far parasitic larvae can be drifted by water currents and how wind speed and the geometry of the water access point can affect larval dispersal, abundance, and distribution is a scientific and public health priority, as, in perspective, it will help to understand how to best target the environmental reservoir of the disease. Recently, the availability of remote imaging technologies like satellites and drones has allowed for the surveying of sites near high infection rates of schistosomiasis. These images can be used to quickly identify markers of high concentrations of infectious parasitic larvae without requiring extensive field campaigns and can also inform hydrodynamic models [20].

Many rivers in areas of high prevalence of schistosomiasis are characterized by thriving and rapidly growing emergent vegetation, typically *Typha* and *Phragmites* spp., that prevent access to the river or lake. Therefore, in the lack of access to clean, piped water, villagers in sub Saharan Africa often need to cut the emergent vegetation to access lake or river waters for the daily chores (such as washing, bathing, fetching water for cooking, watering livestock, etc.). These water access points might differ wildly in their morphology, and their shape changes as emergent vegetation regrows. This may complicate the pattern of flow and affect not only snail distribution but also dispersal, distribution and abundance of the parasite infectious stages for humans [20]. Snails that originate in vegetation upstream can also be entrapped within side ponds, introducing another pathway for infection. Furthermore, circulation patterns within side ponds may retain infectious larvae for long periods of time, increasing the potential window of infection.

Exchange with and circulation within lateral cavities adjacent to open channels has been studied extensively in the laboratory and field as well as through the use of models. It is well established that flow past a lateral cavity results in vortex shedding at the upstream corner of the river interface, turbulent mixing, and the formation of a re-circulation region within the cavity, with the number of vorticies that form being well predicted by the cavity aspect ratio [21–24]. Circulation in a cavity can be driven by river flow, density gradients, or wind. Few, if any, studies have focused on density-driven circulation in a side pond at the river scale. A number of studies have modeled circulation in a side pond in the presence of vegetation. de Oliveira et al. [25] modeled flow in vegetated lateral cavities and found that the flow magnitude within the cavity decreased with increasing vegetation density. They also found that additional circulation zones could form beyond what would be predicted for a non-vegetated lateral cavity of the same aspect ratio. However, a limited range of vegetation densities were tested and the vegetation was uniformly distributed throughout the cavity. Xiang et al. [26] similarly modeled flow in a side pond with uniformly distributed vegetation using a large-eddy simulation (LES) and found that the retention time did not increase monotonically with increased vegetation due to the competition between the formation of shedding vortices at the river interface and the blocking effects of dense vegetation. Lu and Di [27] modeled flow patterns and mass exchange in a lateral cavity both with and without vegetation for a range of cavity aspect ratios. They concluded that the flow velocities within the cavity and mass exchange were more sensitive to the aspect ratio than the vegetation density. Vegetation was placed along the edges and sides of an idealized side pond based on an idealization of the Donghenghe River. However, only one vegetation layout was tested for this site.

Wind can further complicate the flow patterns within a side pond, especially for low-flow or stagnant river, where wind becomes the dominant forcing. Bye [28] numerically solved the Navier–Stokes vorticity equations for a constant applied stress at one end of a rectangular cavity and found that entirely different circulation patterns could arise at

opposing ends of the cavity. Kumagai [29] numerically analyzed wind driven circulation in rectangular cavities with a variety of aspect ratios for a range of wind conditions and found that the number and distribution of circulation patterns depended on both aspect ratio and wind speed. Both studies considered rectangular cavities of uniform depth, and neither included vegetation or bottom friction. Uloa et al. simulated periodic wind-driven resonance in an idealized stratified lake and found that there was a net horizontal transport after a wind cycle. This residual flow was capable of flushing the bottom region of the basin in some cases [30]. This paper focuses on the wind-driven flow within a water access point carved out through the emerging vegetation as a function of vegetation distribution and coverage. To our knowledge, no previous work has focused on wind-driven circulation in vegetated side pond at this scale.

To examine the effects of vegetation and wind on the transport of infectious parasitic larvae in a side pond, an idealized river geometry was modeled using the finite-volume, unstructured SUNTANS model [31]. Two wind directions and a range of wind speeds were tested in combination with two layouts of vegetation patches and a large range of vegetation coverage (0% to ~ 88%).

2 Methods

2.1 Test site geometry

One transmission site along the Lampsar River, an offshoot of the Senegal River near the city of Saint-Louis, Senegal, was chosen as a typical reference case case. As shown in Fig. 1a and b, the site consists of an approximately rectangular section of river with an approximately rectangular man-made lateral section where access to water and infection with schistosome larvae typically occur, from here on referred to also as a side pond for brevity and simplicity. The aspect ratio of the side pond is approximately 0.45. The smaller image in the bottom left shows the same site at a different time of year, in which vegetation had grown to close in much of the side pond. Even in the larger image, vegetation can be seen around the edges of the pond. Thus, to model the effects of vegetation on circulation within the pond, the site was approximated by the idealized geometry shown in Fig. 2, consisting of a rectangular river section and rectangular side pond with an aspect ratio of 0.5.

Fig. 1 Test site along Lampsar River (**a**) and idealization of site as two rectangles (**b**)

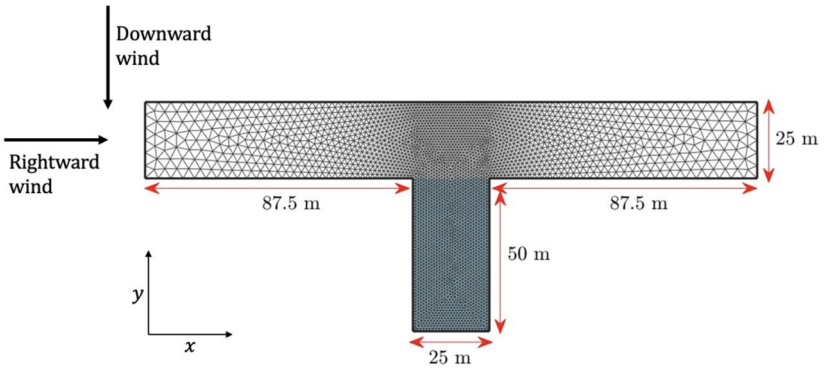

Fig. 2 Grid for idealized Lampsar geometry with the "side pond" shaded in blue. The water access points are along the edges of the side pond, particularly at the bottom edge for Lampsar

The width of the river was made equal to the width of the side pond (25 m) for simplicity. The river section is extended beyond what is visible in Fig. 1a on both ends to minimize model boundary effects. This idealized geometry is meant to represent the simplest form of this site without vegetation, and also allows for more general conclusions to be drawn and applied to other similarly-shaped sites.

2.2 Grid generation and SUNTANS model setup

SUNTANS is a finite-volume Navier–Stokes solver under the Boussinesq approximation with three-dimensional and nonhydrostatic capabilities. For details see Fringer et al. [31]. Figure 2 shows the triangular grid used in SUNTANS, generated with the Mesh 2D package in Matlab [32]. The highest grid resolution is within the side pond with a minimum triangle side length of df = 1 m and a maximum of df = 4.3 m at the edges of the river with a total of 6664 triangles. The maximum depth of the domain was set to 2 m at the center line with a parabolic decrease to a minimum depth of 0.1 m along the shores. The depth of the side pond linearly decreases from 2 m at the river interface to 0.1 m at the bottom edge. These values and profiles were chosen based on personal communications with individuals familiar with the site. Previous studies on similar geometries have shown that lateral cavities with aspect ratios approximately within the range 0.5−1.5 exhibit quasi-2D flow patterns within the cavity, and 3D effects are most prominent along the river interface even in the presence of vegetation [26, 33]. Because we are interested in the bulk flow of parasitic larvae especially within the side pond itself, a 2D depth-averaged model is used. The governing equations solved are the depth-averaged primitive equations. The model was run until velocities in the side pond reached steady state using a time step of $\Delta t = 1\ s$ such that the Courant number $C = U\Delta t/\Delta x$ remained below 1 at all locations, where $U = \sqrt{u^2 + v^2}$ is the velocity magnitude with velocities defined at the centers of each cell and Δx is the distance between cell centers. Because the free-surface height was not of interest in this study, a rigid lid approximation was used to decrease the time required to reach steady state. Velocities within the side pond were plotted as a function of time, and once u and v were no longer changing with time, the model was deemed to be at steady state. This took an average of about 15,000 time steps (about 4 h). The

model was run for 20,000 time steps to ensure that the velocities remained unchanging, and the velocities at the final time step were taken as the steady-state values.

The Lampsar River is generally slow-moving and the water often remains effectively stagnant. Consequently, although there is a small directional flow in the river in reality, all edges of the domain were treated as closed boundaries to examine only wind-driven circulation in the side pond. Assuming the velocity follows a log-law with depth, the bottom drag coefficient on the depth-averaged flow is given by [34]

$$C_{d,b} = \left[\frac{1}{\kappa}\left(\ln\left(\frac{d}{z_0}\right) + \frac{z_0}{d} - 1\right)\right]^{-2}, \tag{1}$$

where $\kappa = 0.41$ is the von Karman constant, d is the depth, and $z_0 = 0.005$ m is the bottom roughness. Although the true bottom roughness at this site is not known, this value is within the typical range found in literature [35].

2.2.1 Vegetation

Both emergent (*Typha* and *Phragmites* spp.) and submerged vegetation (*Ludwigia*, *Ceratophyllum*, and *Potamogeton* spp.) are prevalent and relevant to transmission of scistosomiasis transmission in this area, with submerged vegetation being the more suitable habitat for parastic larvae [6, 20]. Patches of vegetation vary from small approximately circular patches along the shores or scattered throughout the side pond to large masses encompassing most of the center of the pond (see Fig. 1 in [20]). To capture this variability, for each wind direction, model runs were completed with five circular vegetation patches with radii r_{veg} ranging from 0 to 12 m. Vegetation was added to the model by including regions of increased drag on the right-hand side of the momentum equation for the horizontal depth-averaged velocity vector $\vec{U} = \vec{U}(x, y, t)$,

$$\frac{\partial \vec{U}}{\partial t} + (\vec{U} \cdot \nabla)\,\vec{U} = \frac{\vec{\tau}_w}{d} - \overline{C_{d,tot}}\,\frac{\sqrt{u^2 + v^2}\,\vec{U}}{d}, \tag{2}$$

where $\vec{\tau}_w$ is the wind stress and $\overline{C_{d,tot}}$ is the total drag coefficient from bottom and vegetation drag. $\overline{C_{d,v}}$ is the total depth-averaged vegetation drag coefficient

$$\overline{C_{d,v}} = \frac{\alpha_v C_{d,v} p^2 N_a d_v}{2(1 - 0.25 p N_a \pi d_v^2)(1 - \sqrt{N_a} d_v)^2}, \tag{3}$$

where α_v is a shape coefficient taken to be 1 for circular stems, $C_{d,v}$ is the general vegetation drag coefficient, p is the ratio of the height of vegetation to the depth, $N_a = 10,000\ \mathrm{m}^{-2}$ is the number of stems per unit area, and $d_v = 0.005$ m is the characteristic width taken to be the diameter for circular stems [34]. Because exact parameters for the vegetation are not known, N_a is an order of magnitude estimate of the combined densities of *Ludwigia* spp., *Ceratophyllum* spp., and *Potamogeton* spp., the common types of submerged vegetation in the area identified as being correlated with increased prevalence of infectious snails in Wood et al. [20], and the value of d_v is a typical stem width of *Potamogeton* spp. [36–38]. Although the magnitude of the increased drag in the vegetation could be scaled up or down if more accurate parameters were known, we would not expect the structure of the resulting flow to change. For this work, for simplicity, we assumed that the vegetation and its roots spans the entire depth of the water, so that $p = 1$. To avoid abrupt changes in the vegetation

drag coefficient between neighboring grid cells on the edge of vegetation patches, the increased drag was modulated with a smooth function such that

$$C_{d,v} = \frac{C_{d,v0}}{2}\left[1 - \tanh\left(\frac{R - r_{veg}}{d_0}\right)\right], \tag{4}$$

where $C_{d,v0} = 1.5$ is the nominal vegetation drag coefficient as suggested by Zhang [34], r_{veg} is the radius of the vegetation patch which is varied over the range 0–12 m, $d_0 = 0.25$ m is a constant used to control the width of the tanh function, and R is the distance between a cell center and the center of a vegetation patch. In the case where the radius of effect of multiple vegetation patches overlapped, the resulting vegetation drag coefficients were summed together with $C_{d,v}$ capped at a maximum value of $C_{d,v0} = 1.5$. The centers of the five patches of vegetation were chosen such that two patches were centered at the upper corners of the side pond to mimic the widening and narrowing of the river interface seen at different times of the year in Fig. 1a, whereas the remaining three patches were placed randomly throughout the rest of the side pond. To analyze the effect of the configuration of the vegetation patches, the model was also run with a four-patch configuration, in which the patch closest to the lowermost boundary was removed. An example of the four and five-patch configurations is shown in Fig. 3.

A total of seventy-seven SUNTANS simulations were performed as summarized in Table 1. The first two runs compare the effect of wind direction with no vegetation. The next thirty runs vary r_{veg} with five patches for both wind directions. The next thirty runs vary r_{veg} with four patches for both wind directions. The next twelve runs vary wind speed for both patch configurations with a rightward wind. The final three runs are an extension of Runs 3–17 for $r_{veg} = 13$, 14, and 15 m for use in the residence time analysis in Sect. 4.2.2.

2.3 Random walk particle tracking

Each case was run until velocities within the side pond reached steady-state. The steady-state velocity field was then used in a random walk simulation in MATLAB, where the parasitic larvae were treated as passive tracer particles under the assumption that the magnitude of the flow is much larger than the speed at which larvae can swim. The effect of larvae shape is also neglected under the assumption that the passive advection by the mean flow is the dominant driver of particle dispersion at the spatial scale considered here. The inclusion of cercariae behavior and shape would benefit from a three-dimensional model and is left to future work. Although the swimming and sinking of cercariae is generally limited to the vertical dimension, larvae will encounter different horizontal velocities as they move up or down, altering their dispersion beyond what would be predicted by the depth-averaged flow alone [9]. However, cercariae tend to aggregate very close to the air-water interface, generally within the first 1 mm. They alternate between slowly sinking (head-first) at a speed of about 0.1 mm s^{-1} and quickly swimming upward (tail-first) at a speed of about 0.7 mm s^{-1}, spending the majority of their time within 0.5–1 cm from the surface and with no horizontal body first mode in the absence of chemical clues from a potentially susceptible host [7]. Given we treat the parasitic larvae as passive tracers, the effect of temperature on water viscosity, mortality and swimming ability of cercariae is neglected [39]. Future modeling analysis incorporating cercariae motility should also account for the effect of temperature of the free-swimming larvae's behavior. Here, we analyze only the effects of wind and vegetation drag on dispersion in the limit

Table 1 Summary of the model runs

Run #	Description	Wind		Vegetation	
		Direction	Speed ($\mathbf{m/s}$)	# Patches	Patch radius $\mathbf{r_{veg}}$ (m)
1	No vegetation base cases	Right	10	0	–
2		Down	10	0	–
3	Effect of patch radius with rightward wind	Right	10	5	0
4		Right	10	5	0.25
5		Right	10	5	0.50
6		Right	10	5	1
7		Right	10	5	2
⋮		Right	10	5	⋮
17		Right	10	5	12
18	Effect of patch radius with downward wind	Down	10	5	0
⋮		Down	10	5	⋮
32		Down	10	5	12
33	Effect of number of patches with both wind directions	Right	10	4	0
⋮		Right	10	4	⋮
47		Right	10	4	12
48		Down	10	4	0
⋮		Down	10	4	⋮
62		Down	10	4	12
63	Effect of wind speed for five patches	Right	7.07	5	3
64		Right	8.2	5	3
65		Right	10	5	3
66		Right	11.5	5	3
67		Right	12.9	5	3
68		Right	14.14	5	3
69	Effect of wind speed for four patches	Right	7.07	4	3
70		Right	8.2	4	3
71		Right	10	4	3
72		Right	11.5	4	3
73		Right	12.9	4	3
74		Right	14.14	4	3
75	Additional runs for residence time analysis	Right	10	5	13
76		Right	10	5	14
77		Right	10	5	15

where larvae swimming is weak. A number of studies on the tidal dispersion of fish larvae and microalgae have offered insights on particle transport pathways with passive tracer models [40, 41]. Sentchev and Korotenko modeled the dispersion of flounder larvae with both passive tracer particles and active particles incorporating vertical motility. They found that while the active particles generally dispersed more slowly, the horizontal structure of the dispersion predicted with passive particles agreed well with observations [42]. As a first approximation of

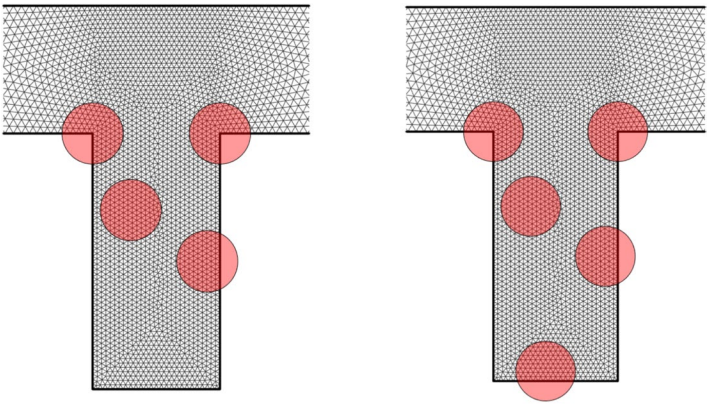

(a) Four-patch layout (b) Five-patch layout

Fig. 3 Example of four- and five-patch vegetation layouts with $r_{veg} = 6$ m. The location of the centers of the patches is the same for all cases

the effect of larvae behavior, results from three additional random walk simulations with the inclusion or particle sinking are shown in the Appendix.

The larvae locations were initialized on the edges of the vegetation patches, as vegetation is a common habitat and breeding ground for the snails [20, 43]. Larvae were placed in a 1 m wide ring around each vegetation patch with a constant density of larvae per unit area for all cases. An example of this initialization for five patches of vegetation with $r_{veg} = 6$ m is depicted in Fig. 4. The position of each particle at time-step n is updated with the random walk

$$x^{n+1} = x^n + \Delta t u^n + \beta_1 \frac{u^n}{U^n} \sqrt{2\epsilon_s \Delta t} + \beta_2 \frac{v^n}{U^n} \sqrt{2\epsilon_t \Delta t}\,, \tag{5}$$

$$y^{n+1} = y^n + \Delta t v^n + \beta_1 \frac{v^n}{U^n} \sqrt{2\epsilon_s \Delta t} + \beta_2 \frac{u^n}{U^n} \sqrt{2\epsilon_t \Delta t}\,, \tag{6}$$

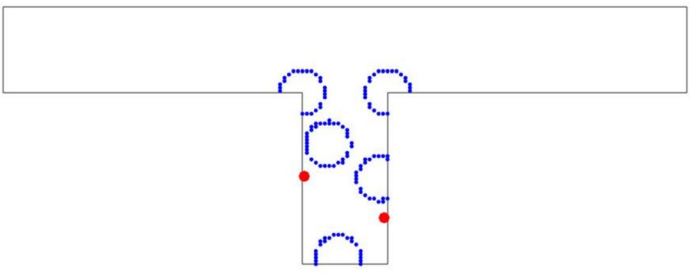

Fig. 4 Example of random walk initialization for five vegetation patches of $r_{veg} = 6$ m with 127 particles. Left and right shore locations where results are discussed are plotted in red

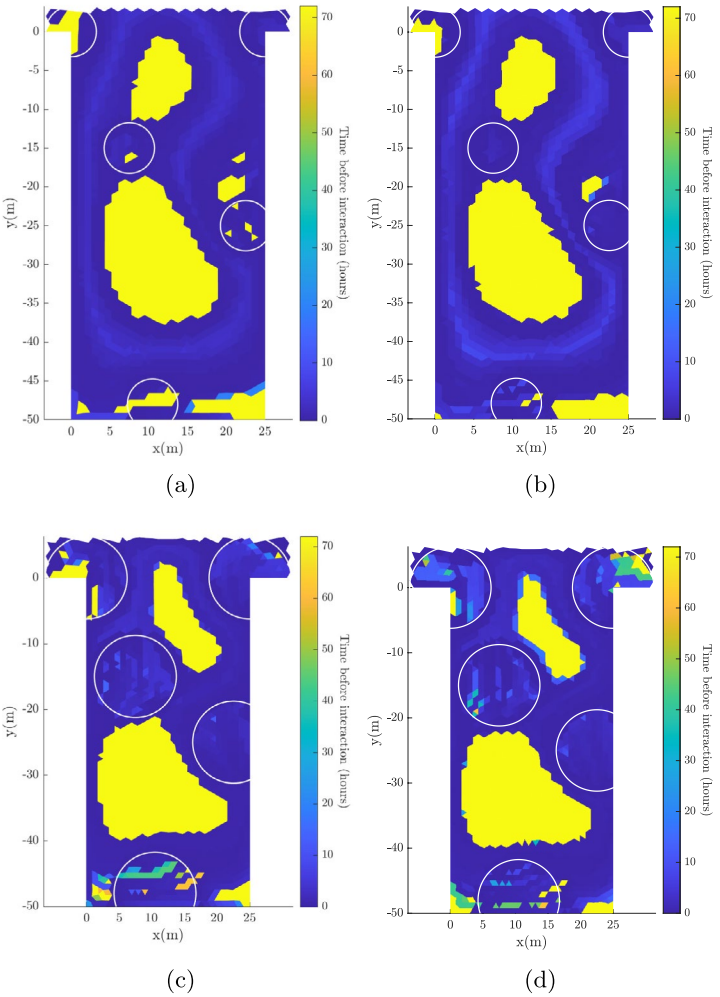

Fig. 5 Comparison between random walk simulation results with interpolation and with a nearest neighbor algorithm for r_{veg} = 3 m (**a, b**) and for r_{veg} = 6 m (**c, d**). All cases shown are with a rightward wind and five patches of vegetation. Interpolated results are shown on the left (**a, c**) and nearest neighbor results are shown on the right (**b, d**)

where β_1 and β_2 are normally-distributed random variables with mean 0 and variance 1 generated for each particle at each time step, and ϵ_s and ϵ_t are the locally streamwise (in the direction of local flow) and transverse (perpendicular to direction of local flow) dispersion coefficients

$$\epsilon_s = 5.93 du^* \,, \tag{7}$$

$$\epsilon_t = 0.15 du^* \,, \tag{8}$$

as suggested by Fischer [44]. Given the idealized geometry in this study and for the sake of generality, the simplest models for shear flow and turbulent dispersion coefficients are used here. Equation 7 gives the shear flow dispersion coefficient assuming a steady logarithmic velocity profile. This is a well-known result originally derived by Elder for the longitudinal dispersion of a passive tracer in a turbulent, infinitely wide channel [45], and has frequently been used to predict the spread of passive tracers in laboratory environments and real systems with finite width [46–49]. However, observations suggest that Elder's dispersion coefficient likely underestimates shear flow dispersion in natural, meandering rivers [50]. Many recent works have suggested more complex expressions for ϵ_t which incorporate parameters such as width and sinuosity or use machine learning to predict dispersion coefficients based on real rivers [51–53]. Equation 8 gives the turbulent dispersion perpendicular to the direction of mean flow determined experimentally for idealized, straight channels, where the coefficient was found to vary from 0.1 to 0.25 with an average value of 0.15 [44]. In natural streams with curvature, this coefficient has been observed in the range 0.4–0.8, with higher values generally indicating more frequent or sharper irregularities in river geometry. Turbulent dispersion in the direction of larvae transport is neglected, as shear flow dispersion tends to be the dominant mechanism in the direction of the mean flow [44].

The friction velocity u^* is calculated with

$$u^* = \sqrt{\frac{\tau_{tot}}{\rho_0}}\,, \tag{9}$$

where the total stress is $\tau_{tot} = C_{d,tot}(u^2 + v^2)$. The total depth-averaged drag coefficient in each cell is taken as the sum of the effects of vegetation and bottom drag such that

$$C_{d,tot} = C_{d,b} + \overline{C_{d,v}}\,. \tag{10}$$

If this update step would place a particle outside the computational domain, the particle is reflected back into the domain by moving it to the inside of the boundary by a distance equal to the normal distance it was outside of the boundary. Each random walk simulation was run for three days with a time step of 1 s. For each time step, the water depth at the location of each particle is taken to be the depth at the nearest cell center, and the u and v velocities of each particle are taken as the steady-state values from the SUNTANS simulations also at the nearest cell center point. As shown in Fig. 5, the effects of linear vs. nearest-neighbor interpolation are negligible.

To determine residence times, particles were initialized throughout the side pond as shown in Fig. 6. Simulations were run with the steady-state velocities from Runs

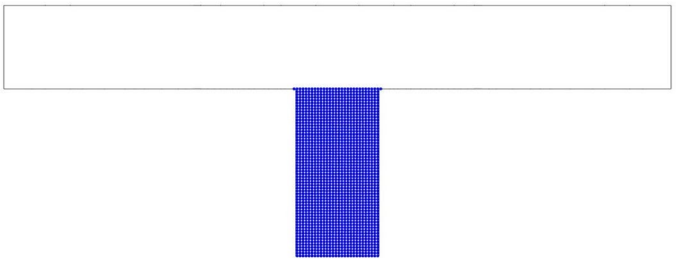

Fig. 6 Random walk initialization for residence time simulations with 1682 particles

63–68 and from Runs 1 and 3–17 to analyze the effect of wind speed and patch radius, respectively. The residence time of each particle was taken as the time at which it first exited the side pond under the assumption that even a small river flow would hinder re-entrainment.

3 Results and discussion

3.1 Steady-state velocity fields

The streamline plots in Figs. 7 and 8 provide a qualitative picture of the resulting steady-state flow fields with different vegetation and wind conditions. With no vegetation, the wind direction strongly affects the flow and velocity magnitudes within the side pond. In the case of a downward wind (Run 2), Fig. 7a shows multiple smaller-scale circulation patterns, with only streamlines in the top 10 m of the pond connecting with the river. As shown in Fig. 7b, a rightward wind (Run 1) results in one large circulation pattern over the entire side pond. Although the recirculation pattern is more complex for the downward wind, the currents are roughly two orders of magnitude weaker.

As shown in Fig. 7, the addition of vegetation significantly changes the flow patterns. The increased drag within vegetation patches creates recirculation regions and flow channelization between the vegetation patches, and the effect is more pronounced for the rightward wind cases. Comparing Fig. 7b–d (Run 8), the effect of vegetation patches is to break up the large-scale recirculation regions seen in the no-vegetation case into multiple smaller-scale recirculation regions. While this effect is less pronounced for the downward wind case (Run 23), the effect of the vegetation on the flow magnitude is more pronounced for the downward wind case.

As shown in Fig. 8, for approximately the same percent coverage, the pattern of vegetation does not appear to significantly alter the flow pattern or magnitude. Comparing Figs. 8b (Run 14) and 8d (Run 47), we see that there is only one dominant circulation pattern near the bottom of the side pond in both rightward wind cases, with the four-patch case allowing for a larger circulation region than the five-patch case. Similarly, comparing Figs. 8a (Run 29) and 8c (Run 62), we see that the circulation zones in the five-patch case are more compacted due to the layout of the vegetation, but overall, the flow pattern and velocity magnitudes are qualitatively similar for both cases.

3.2 Random walk simulations

The motivation of the random walk simulations is to predict the locations in the side pond that are most likely to contain larvae under a set of wind and vegetation conditions. Two measures of the likelihood of larvae being found in a given area are presented: (1) the minimum time before a particle enters each grid cell, which depicts which locations are untouched by larvae throughout the simulation; (2) the total percent of the first 24 h of the simulation time in which each grid cell contains one or more particles, indicating the locations that most consistently contain larvae. With this knowledge, certain areas could be avoided when retrieving water to minimize the risk of infection. Cercariae have lifespans of around 24 h, so results are mainly focused around the first day of the simulations with the full three days being used to discuss residence times [54].

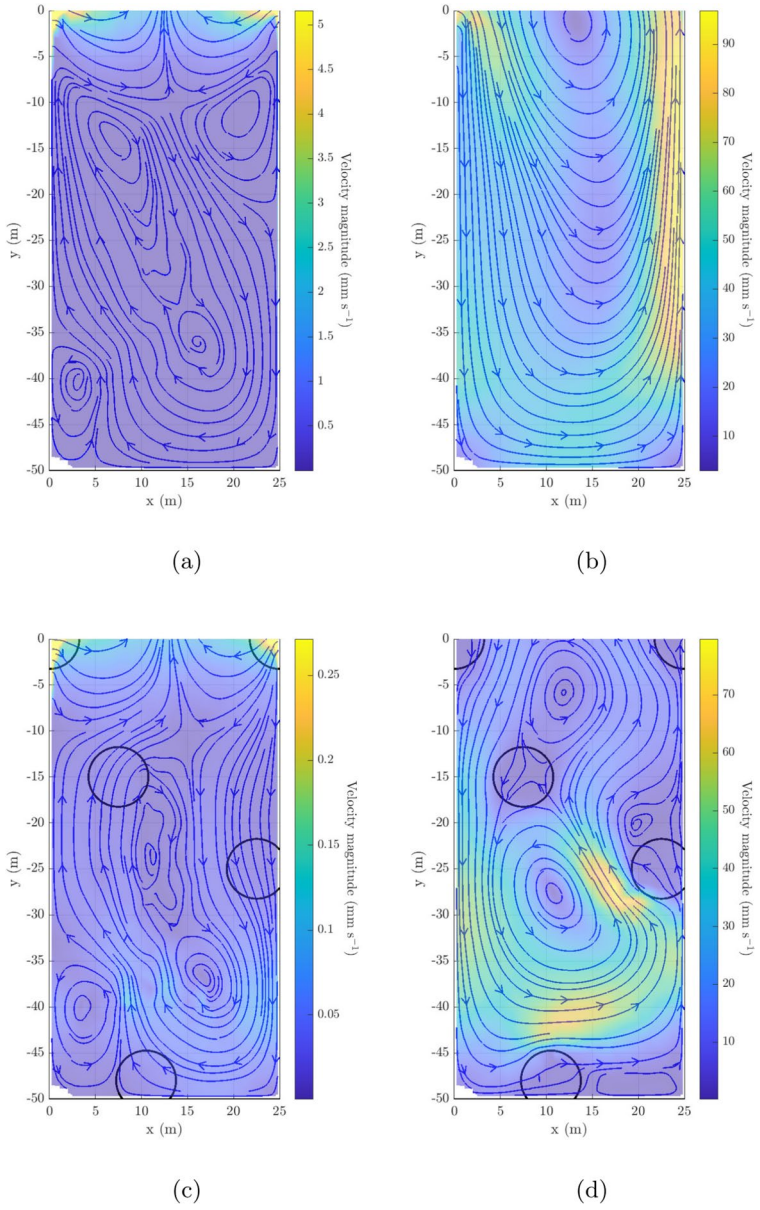

Fig. 7 Streamlines over velocity magnitudes for **a** a downward wind with $U_{10} = 10$ m s^{-1} with no vegetation (Run 2), **b** a rightward wind with $U_{10} = 10$ m s^{-1} with no vegetation (Run 1), **c** a downward wind with five $r_{veg} = 3$ m vegetation patches (Run 23), and **d** a rightward wind with five $r_{veg} = 3$ m vegetation patches (Run 8). Panels in the left column represent a downward wind and in the right column a rightward wind

A series of snapshots from the random walk simulations initialized as shown in Fig. 6 allowing for re-entrainment are shown in Fig. 9. With no vegetation and a rightward wind (Fig. 9a), the particles quickly arrange into a large-scale circulation pattern seen in the

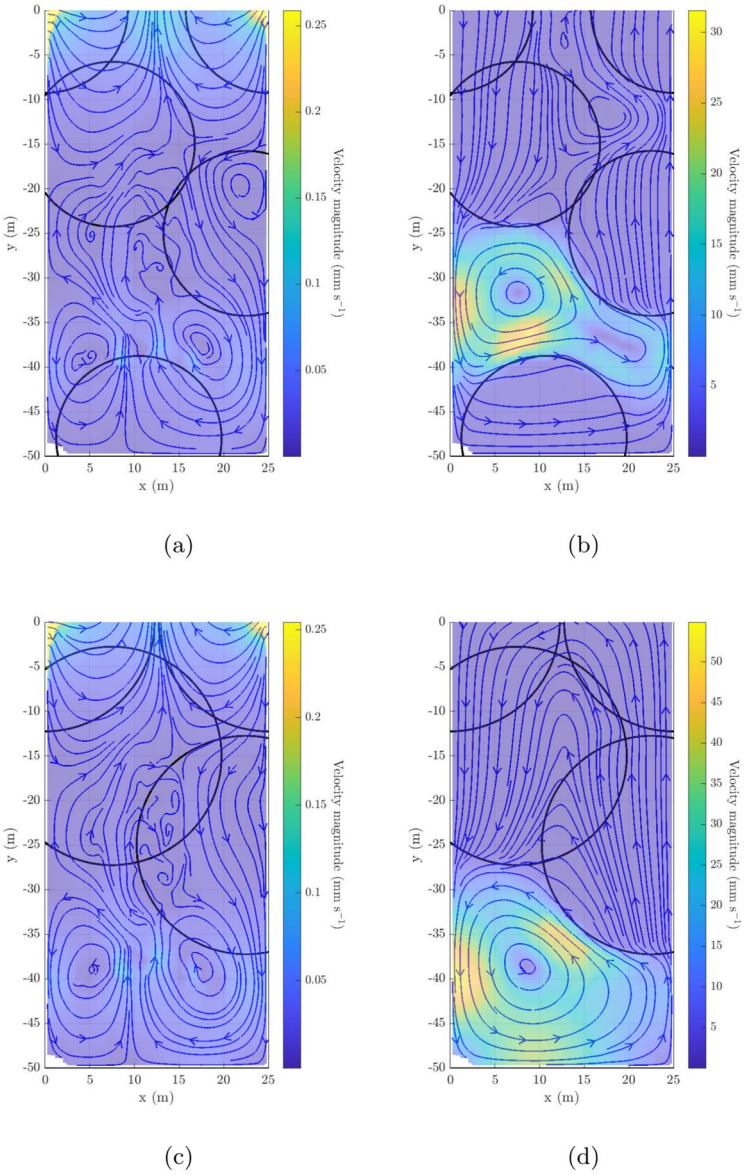

Fig. 8 Streamlines over velocity magnitudes for **a** a downward wind with five r_{veg} = 9 m vegetation patches (Run 29), **b** a rightward wind with five r_{veg} = 9 m vegetation patches (Run 14), **c** a downward wind with with four r_{veg} = 12 m vegetation patches (Run 32), and **d** a rightward wind with four r_{veg} = 12 m vegetation patches (Run 17). Panels in the left column represent a downward wind and in the right column a rightward wind. The five-patch cases (top) have 65% area coverage and the four-patch cases (bottom) have 64% area coverage

streamlines in Fig. 7b. After one day, we see that effectively all of the particles have exited the side pond. Figure 9b shows snapshots from the same time steps for a rightward wind with five r_{veg} = 3 m vegetation patches. With the added vegetation, large-scale circulation

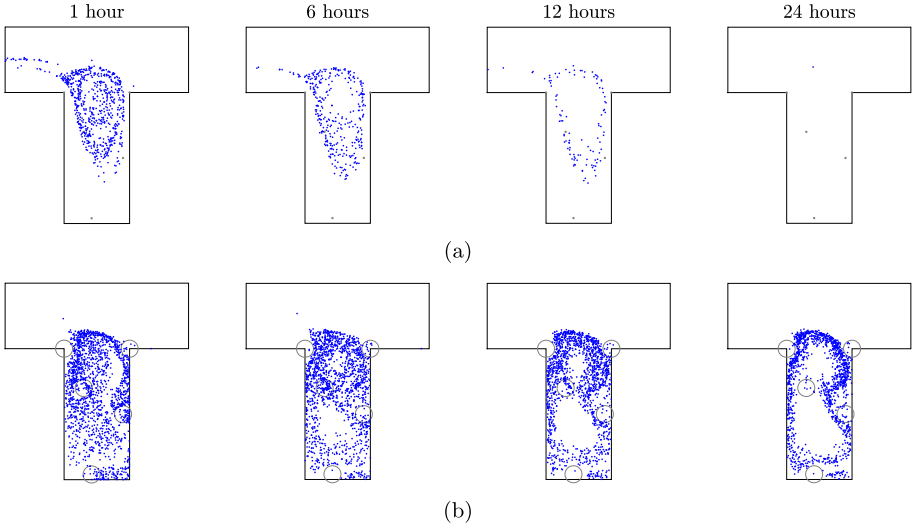

Fig. 9 Random walk simulations for the initialization shown in Fig. 6 after 1, 6, 12, and 24 h for a rightward wind with no vegetation (**a**) and with five patches of $r_{veg} = 3$ m vegetation (**b**)

patterns take longer to form and particles take longer to exit, with many remaining in the in the domain after one day has passed.

3.2.1 Effect of wind direction and magnitude

The results of the random walk particle tracking simulations for the cases with five $r_{veg} = 3$ m vegetation patches are shown in Fig. 10. Figure 10a and b show the time before a particle entered each grid cell over the first 24 h of the random walk simulation for a downward wind and a rightward wind, respectively. Figure 10c and d show the total percent of time that each grid cell contained one or more particles for the same two cases. As before, for the same percent coverage and vegetation layout, far more of the side pond is sampled by particles in the rightward wind case than in the downward wind case. For a downward wind, the particles remain close to the vegetation, only reaching grid cells up to about 5 m away from their starting vegetation patch in the course of one day. In contrast, for a rightward wind, the starting locations of the particles are difficult to surmise based only on Fig. 9b. The faster velocities in this case allow for the particles to quickly travel away from their vegetation patches and be entrained into the large-scale flow patterns shown in the streamline plot for the same case in Fig. 7d. However, the areas that are sampled by the particles in the downward wind case are nonempty for the majority of the simulation, whereas every cell in the rightward wind case is nonempty for less than 25% of the 24 h. This suggests that although there are very few locations to avoid parasitic larvae in a rightward wind case, the chance of a long-term interaction is more likely with a downward wind.

As for wind speed, the time before a particle first reaches a cell along the left shore and another along the right shore for a range of U_{10} values are shown in Fig. 11. The locations of these cells are shown in Fig. 4. The points were arbitrarily chosen along the shore where a person is most likely to enter the side pond. At Lampsar specifically, the

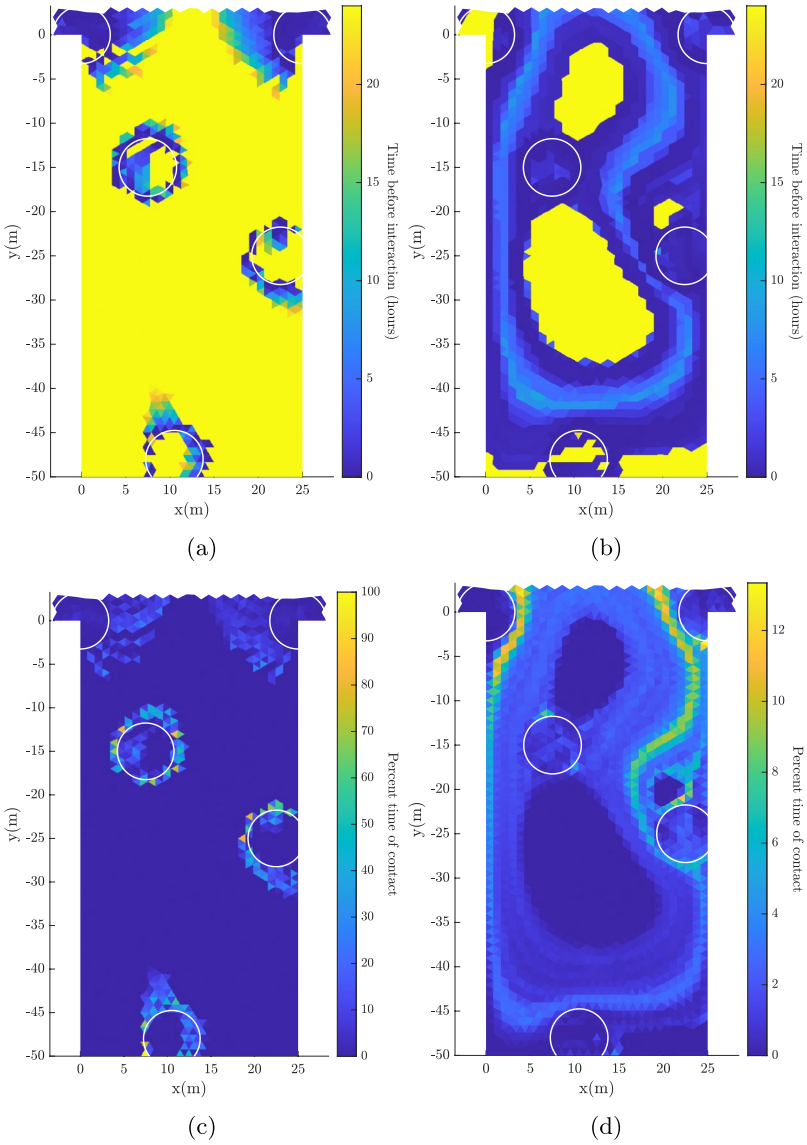

Fig. 10 Time before a particle first enters each grid cell (top) and total percent time during which each grid cell is nonempty (bottom) during the first 24 h of a random walk simulation with a downward (**a, c**) and rightward (**b, d**) wind with five $r_{veg} = 3$ m vegetation patches. Panels in the left column represent a downward wind and in the right column a rightward wind

most common access point is along the bottom of the side pond. However, in order to capture the widest range of r_{veg} before the chosen locations intersect with a vegetation patch, two points along the longer dimension of the side pond were chosen under the assumption that similar trends would hold for any point along the edge. All cases were run with four and five vegetation patches of radius 3 m and rightward applied wind. The time before first contact with both grid cells decreases monotonically with increased U_{10}

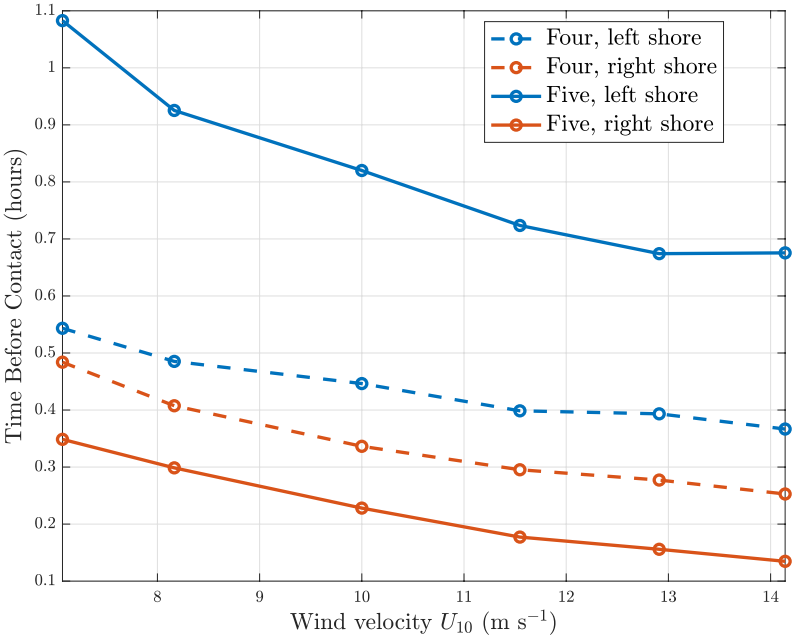

Fig. 11 Time before a particle first entered a grid cell along the left shore located at $y = -25$ m (dashed line) and a cell along the right shore located at $y = -36$ m (solid line) for a range of U_{10} values from 7.07 to 14.14 m s^{-1}. The locations of these two cells is shown in Fig. 4. A rightward wind is applied in all cases with 3 m radius vegetation in four patches shown in blue and five patches shown in red

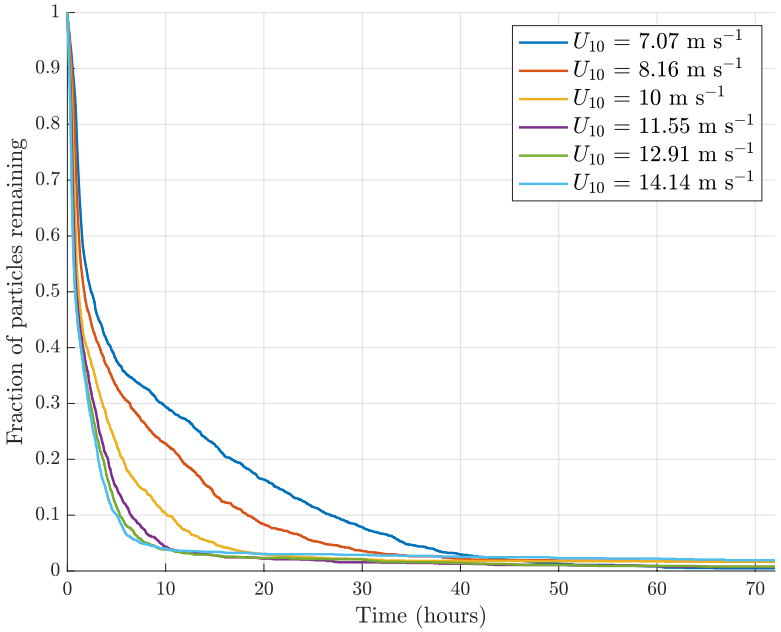

Fig. 12 Fraction of particles remaining in the side pond as a function of time for each U_{10}

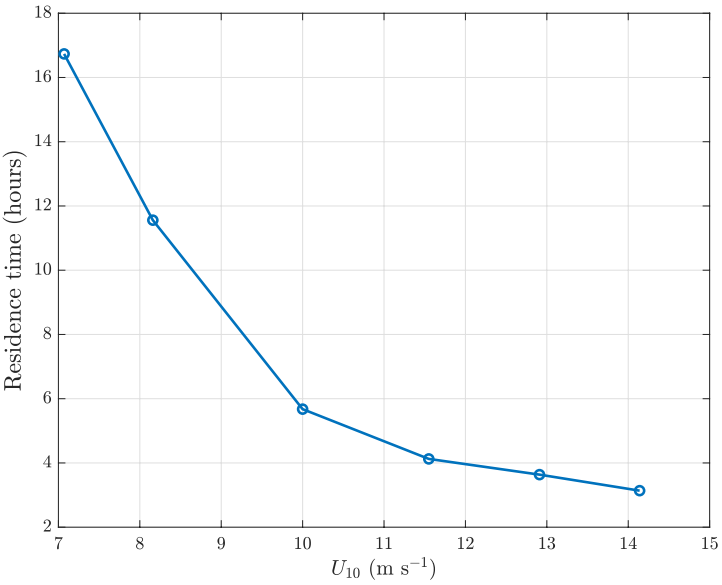

Fig. 13 Time after which less than twenty percent of the particles initialized in Fig. 6 are remaining in the side pond as a function of wind speed

with both four and five patches of vegetation, with four patches resulting in longer time before contact for all U_{10} values.

The fraction of particles remaining in the side pond over the course of the full three-day residence time random walk simulations is plotted in Fig. 12 for each of the U_{10} values. Although the fraction of particles in the side pond decreases monotonically with time for all cases, the decay is not quite exponential, especially for the faster wind speeds. Jackson et al. [23] presented empirical models for residence time in a lateral cavity incorporating a number of characteristic parameters such as cavity width, length, Reynolds number, and roughness, but their models did not include wind nor vegetation and thus cannot be applied here. For simplicity and for the sake of comparison, the residence time of each case was taken to be the time after which 20% or fewer of the particles were remaining in the side pond. As shown in Fig. 13, the residence time decreases monotonically with increased wind speed.

Although a constant wind stress was applied in these simulations, in reality, wind magnitude varies over the course of a day even in the presence of persistent monsoons. Winds in coastal Senegal tend to follow a diurnal cycle of one to two daily wind events, with the duration and strength of events varying seasonally from a few hours to half a day [55]. The duration, direction, and strength of wind events is a parameter space to be explored in future works. As a first approximation of the effect of unsteady winds on particle dispersion, additional model runs were completed with an idealized unsteady wind pattern. Details of these runs and results are given in the Appendix. Unsteady winds lead to increased residence times with the most pronounced effect on the largest patch radii case. Based on these results, the ratio between the steady-wind residence time and wind event duration is a good indicator of the effect of wind unsteadiness. We would expect that the residence time increases when the wind duration relative to

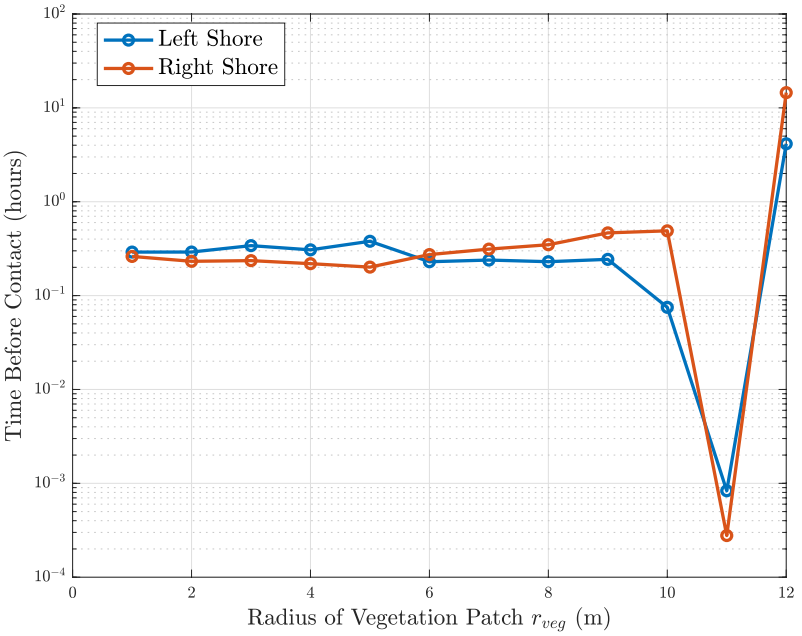

Fig. 14 Time before a particle first entered a grid cell along the left shore located at $y = -25$ m (blue) and a cell along the right shore located at $y = -36$ m (red) for 5 patches of vegetation with radii ranging from 0 to 12 m. The locations of these two cells are shown in Fig. 4

the steady-wind residence time decreases, although that would need to be quantified in a future study. Additionally, wind direction in this area varies seasonally but is rather constant over the course of a month [55]. In future works, wind directions could also be varied over the course of a simulation based on a local wind rose for a season of interest.

3.2.2 Effect of vegetation coverage and layout

As for the effects of vegetation patch radius r_{veg}, the time before a particle first reaches the same two cells along the right and left boundaries for a range of radii are shown in Fig. 14. Again, all cases have five vegetation patches and a rightward applied wind with $U_{10} = 10$ m s^{-1}. For both locations, the time before first contact is less than one hour for $r_{veg} < 12$ m and does not change monotonically with an increase in radius, unlike the case with varying wind speed. The time before contact decreases when $r_{veg} = 11$ m for both locations, as the initialized edge of a vegetation patch intersects both points of interest for this radius. For the radii less than 11 m, we see both increases and decreases in time before first contact for a unit increase in patch radius as a result of the competition between the shift in starting position of particles towards or away from the cells of interest as the patch radius changes and the overall slowing of the flow velocity as the patch radius increases.

The fraction of particles remaining in the side pond over the course of the residence time random walk simulations is plotted in Fig. 15 for each of the r_{veg} values. As with the varied wind speed cases, not every vegetation patch radius results in exponential decay of the number of particles in the side pond over time. Again, for simplicity, the

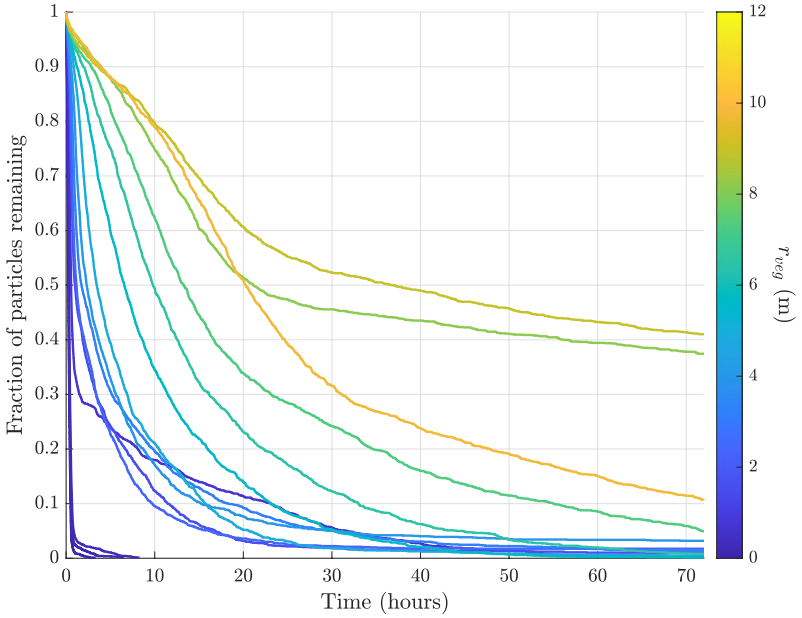

Fig. 15 Fraction of particles remaining in the side pond as a function of time for each r_{veg}. The color of each curve corresponds to the value of r_{veg} in each simulation, with smaller patch radii in blue and larger patch radii in yellow

residence time of each case was taken to be the time after which 20% or fewer of the particles were remaining in the pond. As shown in Fig. 16a, the steady-state velocity magnitude averaged over the side pond $\overline{U}$ decreases monotonically with increased r_{veg} for both wind directions. However, as shown in Fig. 17, the residence time does not decrease monotonically with increased patch radius for a rightward wind. For this analysis, an additional three simulations with larger patch radii (Runs 75-77 for r_{veg} = 13, 14, and 15 m) were completed to capture the full range of residence time behavior. There appear to be five regimes based on the size of the vegetation patch: Regime 1 ($0 \leq r_{veg} < 1$ m), Regime 2 ($1 \leq r_{veg} < 6$ m), Regime 3 ($0 \leq r_{veg} < 9$ m), Regime 4 ($9 \leq r_{veg} < 12$ m), and Regime 5 ($r_{veg} \geq 12$ m). The boundaries of these regimes are highlighted in Fig. 17. In Regime 1, the residence time increases exponentially with increased patch radius from 0 to 1 m. As r_{veg} increases into Regime 2, there is an order of magnitude increase in residence time, which then remains approximately constant. In Regime 3, there is a return to approximately exponential increase in residence time with increased patch radius. In Regime 4, there is another order of magnitude increase in residence time to the maximum of about 9 days for r_{veg} =10 m, which remains approximately constant when r_{veg} = 11 m before decreasing by an order of magnitude for r_{veg} = 12 m. Finally, in Regime 5, the residence time is near constant for $r_{veg} \geq 12$ m.

The lower circulation region first forms at r_{veg} = 1 m, which explains the sharp increase in residence times from r_{veg} = 0.5 to 1.0 m, marking the transition from Regime 1 to Regime 2. In Regime 2, the rate at which particles leave the side pond is limited by the diffusive time scale, as any particle entrained into the circulation region will only exit the pond due to the diffusive component of the random walk which allows for particle transport

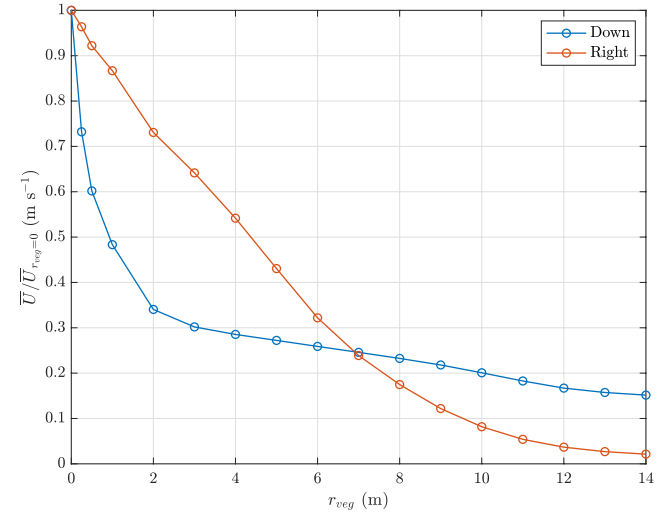

(a)

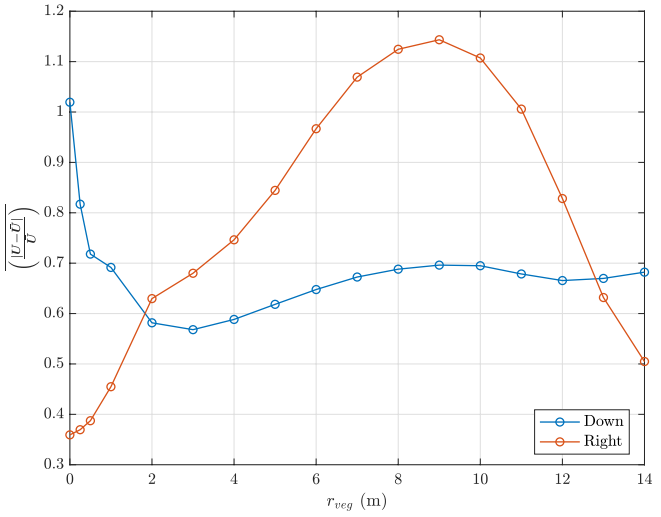

(b)

Fig. 16 Mean steady-state velocity magnitude normalized by the mean steady-state velocity for $r_{veg} = 0$ m (**a**) and normalized deviation in velocity magnitude (**b**) as a function of patch radius r_{veg} for a rightward wind (red) and downward wind (blue) with five vegetation patches (Runs 3–32)

normal to the streamlines. At $r_{veg} = 6$ m, the smaller top circulation region stretches into the river. Now, in Regime 3, as particles are entrained into this top circulation region, they exit into the river on an advective rather than diffusive timescale, so there is a return to exponential increase in residence time as a function of patch radius due to the overall decrease in velocity magnitude as more vegetation is added. At $r_{veg} = 9$ m, marking the

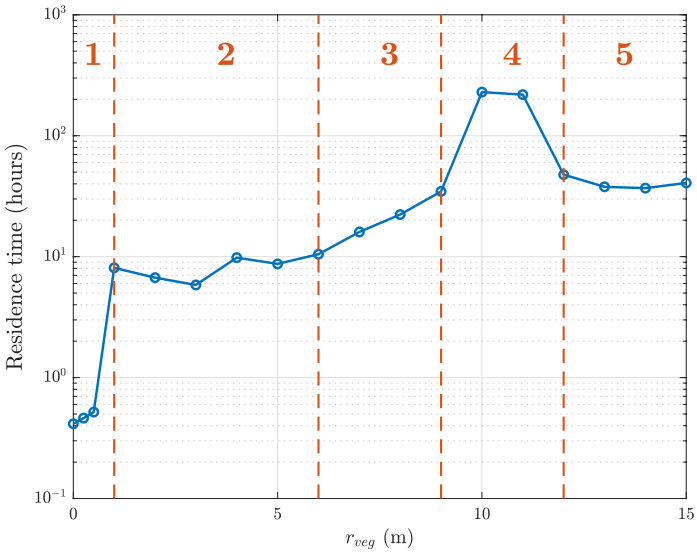

Fig. 17 Time after which less than twenty percent of the particles initialized in Fig. 6 are remaining in the side pond as a function of patch radius for a rightward wind with five vegetation patches. The five regimes are labeled and demarcated with dashed red lines

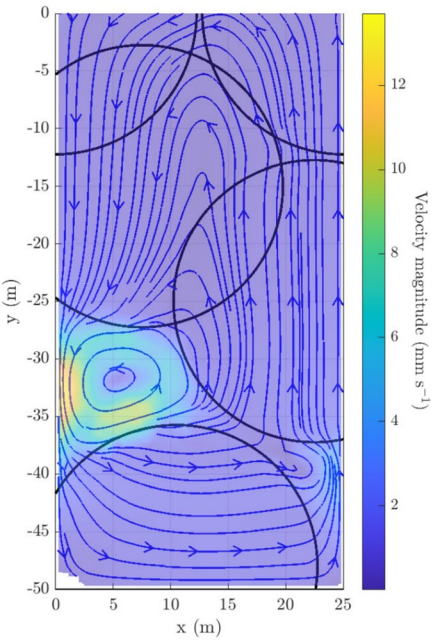

Fig. 18 Streamlines over velocity magnitudes for a rightward wind with five $r_{veg} = 12$ m vegetation patches (Run 17). With this amount of vegetation coverage, only one circulatory structure encompasses the entire side pond

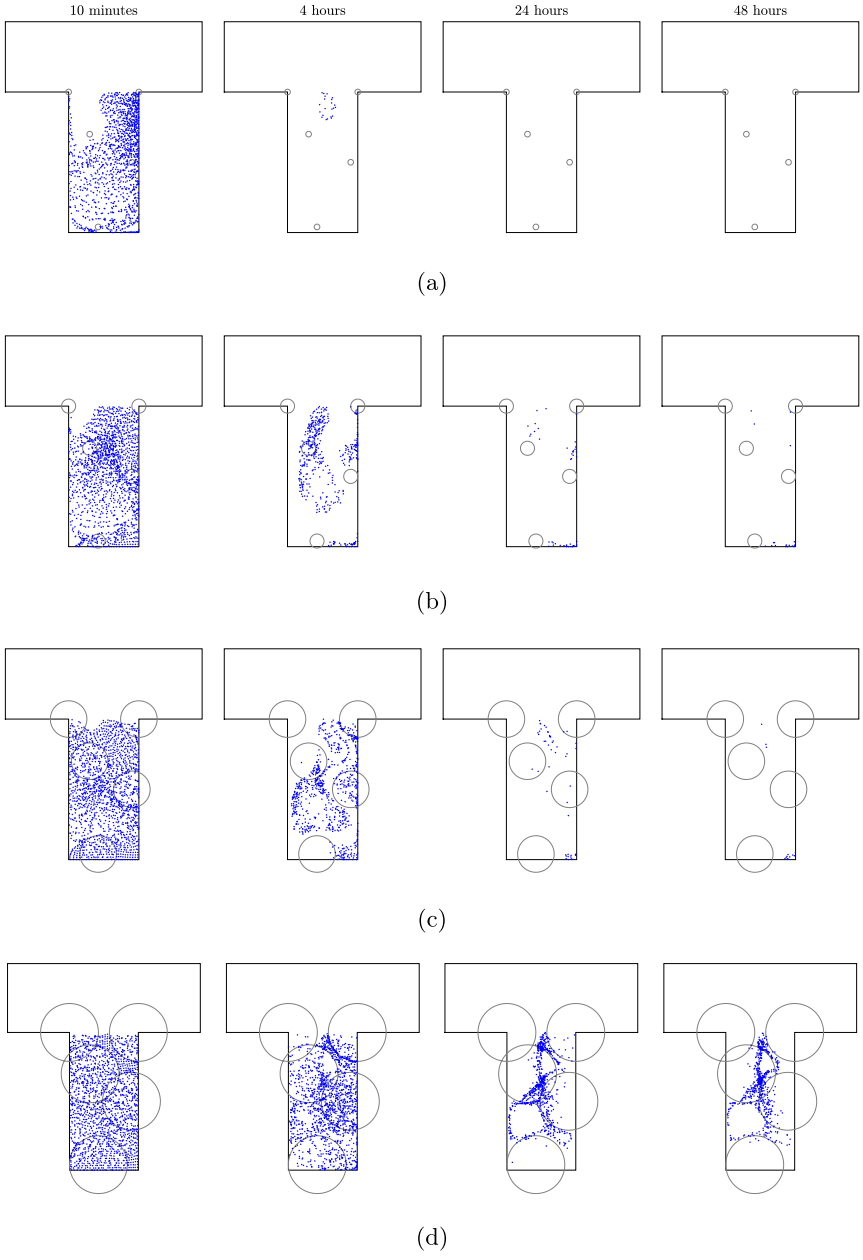

Fig. 19 Random walk residence time simulation for the initialization shown in Fig. 4 after 10 min, 4 h, 24 h, and 48 h for a rightward wind with five patches of vegetation with $r_{veg} = 0.5$ m (**a**), $r_{veg} = 2$ m (**b**), $r_{veg} = 6$ m (**c**), and $r_{veg} = 10$ m (**d**)

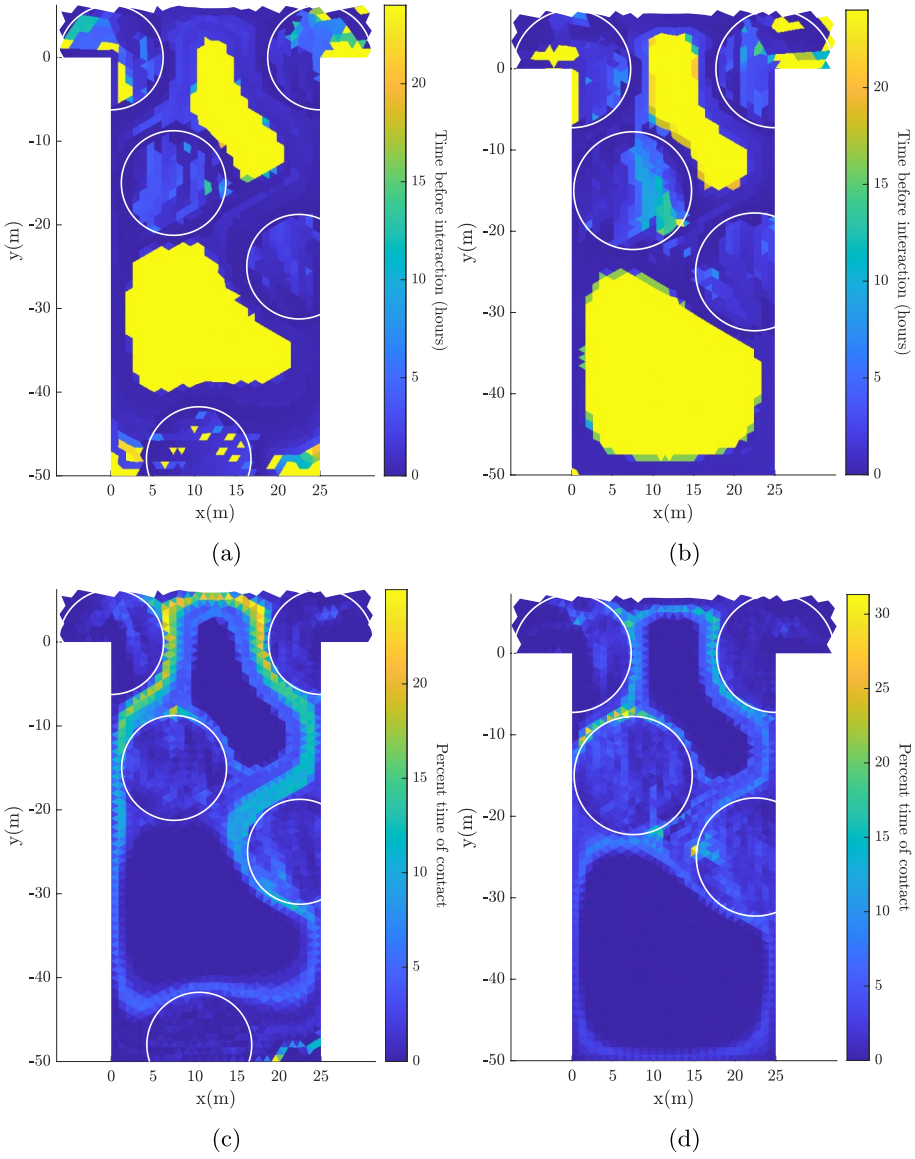

Fig. 20 Time before a particle first enters each grid cell (top) and total percent time during which each grid cell is nonempty (bottom) during the first 24 h of a random walk simulation with rightward wind for two vegetation patch layouts with a comparable fractional coverage: Five patches with $r_{veg} = 6$ m (**a, c**) and four patches with $r_{veg} = 7$ m (**b, d**). The five-patch configuration (left) has 36% vegetation area coverage and the four-patch configuration (right) has 35%

beginning of Regime 4, the two middle vegetation patches intersect, covering the pathway from the lower circulation region to the river. At $r_{veg} = 10$ m, the upper circulation pattern closes off from the river, and these two effects act to sharply increase the residence time, as particles entrained into the circulation regions again exit into the river on the diffusive

timescale. Finally, at $r_{veg} = 12$ m, the upper and lower circulation patterns merge, such that there is only one circulatory structure encompassing the entire side pond, as can be seen in Fig. 18. Increasing the patch radius beyond $r_{veg} = 12$ m in Regime 5 has little effect on the overall drag because the vegetation is essentially uniformly distributed throughout the side pond (recall that the drag coefficient where vegetation overlaps is capped at a maximum value of $C_{d,v0} = 1.5$). The uniform distribution of drag leads to one large circulation pattern that does not change with increasing patch radius, thus leading to a relatively constant residence time.

Figure 19 shows snapshots of the random walk simulations after 10 min, 4 h, 1 day, and 2 days for one vegetation patch radius in each of the first four regimes: $r_{veg} = 0.5$ m (Regime 1), 2 m (Regime 2), 6 m (Regime 3), and 10 m (Regime 4). Not only is the number of particles at each time step vastly different between the different regimes, but the spatial variability of the remaining particles varies significantly as well. For example, a more closed off circulation pattern has formed in the Regime 4 case than in Regime 3. Additionally, although there is a subset of particles trapped in the lower right corner for Regimes 2 and 3, no particles remain in the same corner after 48 h for Regimes 1 and 4.

Looking now at the mean normalized velocity magnitude deviations plotted in Fig. 16b, the normalized deviation in velocity magnitude $U' = \overline{(U - \overline{U})/\overline{U}}$ changes significantly with changes in r_{veg} with a maximum of about 1.1 at $r_{veg} = 9$ m for a rightward wind. At this patch radius, strong velocity deviations suggest large recirculation zones in which the flow is significantly different than the average. Above $r_{veg} = 9$ m, the deviations decrease, suggesting the recirculation zones may be weakening. Although the maximum residence time in Fig. 17 occurs with $r_{veg} = 10$ m, the approximate trend in velocity deviations as a function of r_{veg} qualitatively matches that of the residence times. Both Figs. 17 and 16b suggest that there is an optimal range of r_{veg} values in which the recirculation patterns are the strongest and the residence times are the longest. The entrainment of particles by circulation regions closed off from the river, corresponding to increasing velocity deviations, increases residence times beyond what would be seen if an averaged vegetation drag was applied uniformly over the side pond. The formation and movement of these regions as r_{veg} varies results in the behaviors seen in the five regimes in Fig. 17. As the vegetation approaches near full-coverage of the pond (about 88% by area, corresponding to $r_{veg} =$ 12 m), the effect of spatial variability in the increased drag becomes minimal, and the residence time decreases from the maximum seen at $r_{veg} = 10$–11 m.

3.2.3 Effect of number of vegetation patches

The number of vegetation patches does not appear to have as significant of an effect on the qualitative nature of the flow within the side pond as do wind direction and magnitude or patch radius. Figure 20 shows the time before a particle entered each grid cell for five 6 m radius patches (Fig. 20a) and for four 7 m radius patches (Fig. 20b), which have comparable vegetation coverages of 35.9% and 35.3%, respectively. Figure 20a appears very similar to Fig. 20b in that for a similar percent coverage, both vegetation layouts have a large portion of the side pond that is quickly sampled by one or more particles and two large regions in which particles do not enter over the course of the first 24 h of the simulation near the upper-right and lower-left corners. These unsampled regions are smaller in the five-patch case than the four-patch case due to distribution of vegetation, but qualitatively, the results are similar.

As shown in Fig. 20c and d, the total fraction of the simulation time during which each grid cell contained one or more particles is also similar for both vegetation layouts in terms of both structure and magnitude. The majority of the side pond is nonempty less than 5% of the time with a band of cells that contain one or more particles up to 30% of the time. The existence of the lowest patch in the five-patch case limits the span of this band in the y direction, and we also see a higher percent time of contact at the river interface in the five-patch case than in the four-patch case. Overall, however, the effect of changing the layout of vegetation appears to be minimal.

4 Conclusions

The circulation of Schistosome larvae in a vegetated side pond was modeled under a range of wind and vegetation conditions to better understand their transport in a side pond adjacent to the Lampsar River in Senegal. Knowledge of the likelihood of finding infectious larvae in a given area can be a valuable tool in preventing schistosomiasis. The results show that including vegetation in the model significantly alters the resulting structure and magnitude of wind-driven flow. Changing the vegetation layout did not have a strong effect on the results, whereas increasing patch radius decreased velocity magnitudes, generally increased residence times, and allowed for the formation of recirculation regions while also introducing more areas for snail-supporting vegetation. The five regimes of residence times for ranges of patch radii suggest that advective and diffusive timescales are interacting to give varied flow behavior due to the relationships between patch radius and drag, dispersion, velocity magnitude, and velocity deviations. Changing wind direction gave the largest difference between otherwise identical model runs, with downward winds resulting in more complex circulation patterns but slower velocities than rightward winds. Increasing wind magnitude increased flow velocities but did not significantly alter the structure of the flow.

Under the drag generated by wind alone, we find that infectious stages of the parasites can disperse several tens of meters away from where infected snails shed them. Our simulations provide a mechanistic explanation of why the spatial scale at which infection can occur is wider than previously conceived and in accordance with our correlative studies such as Wood et. al [20] and Jones et al. [56]. A relevant implication of this finding is that any environmental intervention considered, be it through the use of molluscicides [57], biological control [3, 5], or vegetation removal [6], should occur at a scale of about hundreds of meters from water access points. We also find that patches of increased drag in a lateral cavity can lead to the formation of multiple recirculation patterns beyond what would be predicted based on cavity aspect ratio alone or with the inclusion of uniformly distributed added drag. The seasonal patch-like vegetation seen at sites like Lampsar likely cause strong recirculation regions to form in water access points, leading to increased residence times of infectious parasitic larvae. The model presented here could be used to inform the targeted removal of vegetation patches for conditions where larvae residence times are likely to be maximized as well as to inform local residents of the visual indicators of high larvae concentrations.

4.1 Model limitations and future work

The model presented here provides a framework to predict the effect of wind and vegetation on dispersion rates and patterns of idealized parasitic larvae but should be refined further to accurately predict transport in a specific site of interest. Future models aimed at predicting cercarial dispersion at a fine spatial scale should account for the actual river morphology and bathymetry. Incorporating the vertical motility of larvae and their swimming performance and life expectancy as a function of temperature into future models could provide further insight into their fate and transport. The ellipsoidal shape of cercariae should also be incorporated in future works. The degree of alignment of a larva's principal axis with the primary direction of flow could introduce increased form drag and alter dispersion pathways. Including more accurate wind and vegetation parameters would likely also increase the applicability of the results to the specific model test site. Observational wind speed and direction data could be used as inputs to model runs to capture real-world wind variability and resulting transient flow effects. Similarly, vegetation parameters were uniformly applied based on the combined properties of common submerged vegetation found in the area. The inclusion of emergent vegetation and spatial variation of stem characteristics and the height of submerged vegetation relative to the local depth using precision mapping could more accurately capture the range of vegetation seen at sites like Lampsar. Additionally, repeating the same analysis for more sites and more vegetation layouts could allow for more general conclusions to be drawn about the transport of Schistosome larvae in vegetated areas. A three-dimensional model could also be considered to best capture the dynamics at the river interface, especially in more complicated geometries or if including river flow.

Appendix

Unsteady wind

Additional model runs with five patches of vegetation and a rightward wind were completed with the idealized periodic wind cycle

$$U_{10}(t) = \max\left(U_{10,\max}\cos\left(\frac{2\pi t}{T_{\text{wind}}}\right), 0\right), \tag{11}$$

where $U_{10,\max} = 10$ m s^{-1} and the wind event timescale T_{wind} was taken to be 6 h. This gives two six-hour wind events per day, a pattern similar to the monthly average seen in spring and summer at the study site [55]. Three patch radii were chosen based on their steady wind residence times from Fig. 17 relative to T_{wind}: $r_{veg} = 0.5$ m ($< T_{\text{wind}}$), $r_{veg} = 3$ m ($\approx T_{\text{wind}}$), and $r_{veg} = 8$ m ($> T_{\text{wind}}$). The model was run for 6 h with a constant $U_{10} = U_{10,\max}$ to allow for initial spin up, after which time the wind forcing varied according to Eq. 11 for an additional three days. Random walk simulations began after the initial 6 h period. For comparison with the steady wind cases, simulations were run without re-entrainment for up to three days or until less than 1% of the particles remained in the side pond. The fraction of particles remaining in the side pond over the course of the random walk simulations is plotted in Fig. 21 for each of the three r_{veg} values along with the comparable steady wind cases from Fig. 15. The residence time, taken to be the time after which less than twenty percent of the initialized particles are remaining in the side pond, are given in Table 2. Residence times increase with unsteady wind forcing for all three patch radii. Particles leave

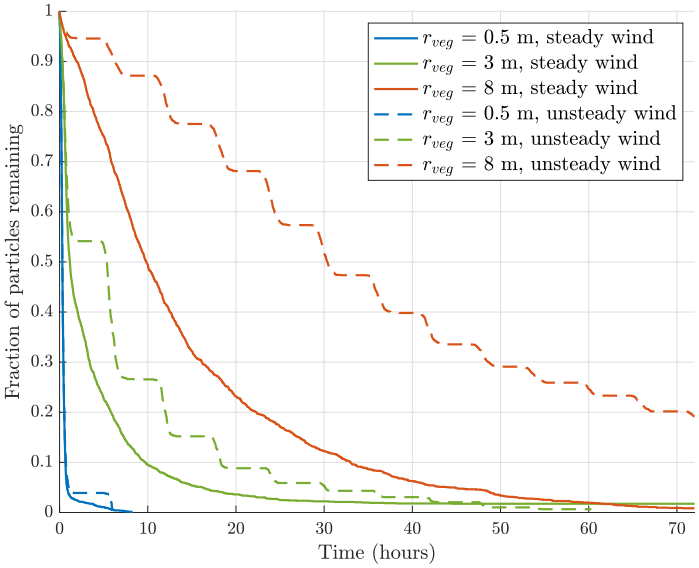

Fig. 21 Fraction of particles remaining in the side pond as a function of time for each of the three r_{veg} values tested with unsteady wind forcing. Unsteady results are plotted with dashed lines. Steady wind results are plotted with solid lines and are taken from Fig. 15. The color of each curve corresponds to the value of r_{veg} in each simulation

Table 2 Comparison between residence times with a steady wind forcing and with the periodic wind forcing given in Eq. 11

r_{veg} (m)	Steady wind residence time (hours)	Unsteady wind residence time (hours)
0.5	0.52	0.54
3	5.84	12.02
8	22.30	71.38

Steady wind residence times are taken from Fig. 17

the side pond most efficiently when the periodic wind forcing is at its maximum, leading to the stair-stepped patterns seen in the unsteady curves in Fig. 21. For $r_{veg} = 0.5$ m, the increase in residence time is minimal, as most particles exit the side pond during a single wind event. With $r_{veg} = 3$ m, roughly half of the particles exit the side pond during the first wind event, but the remaining particles are slower to exit than in the steady wind case due to the periodic low wind periods. $r_{veg} = 8$ m has the largest increase in residence time, as the steady wind flushing time is much longer than T_{wind}.

Particle sinking

Additional random walk simulations were run with particle sinking. Larvae were initialized at the surface and given a constant sinking speed of $w_{sink} = 0.1$ mm s^{-1}, the average value

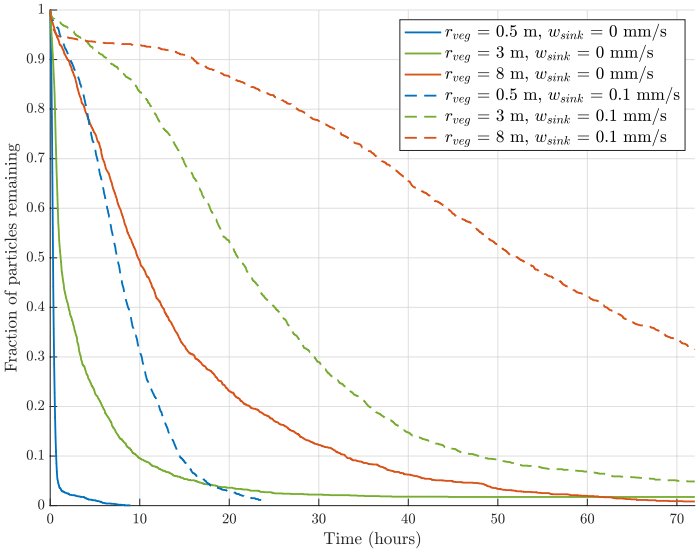

Fig. 22 Fraction of particles remaining in the side pond as a function of time for each of the three r_{veg} values tested with particle sinking. Sinking results are plotted with dashed lines. Passive tracer results are plotted with solid lines and are taken from Fig. 15. The color of each curve corresponds to the value of r_{veg} in each simulation

Table 3 Comparison between residence times with passive tracer particles and with sinking particles

r_{veg} (m)	Passive tracer residence time (hours)	Sinking residence time (hours)
0.5	0.52	12.16
3	5.84	35.63
8	22.30	91.04

Passive tracer residence times are taken from Fig. 17

observed by Krishnamurthy et al. [7]. The velocity profile was assumed to be logarithmic with depth in the direction of mean flow such that

$$U(z) = \frac{u^*}{\kappa} \ln\left(\frac{z}{z_0}\right), \tag{12}$$

where $U(z)$ is the velocity magnitude at height z above the bed and u^* is given by Eq. 9. The average depth of the side pond is 0.9 m, meaning in the absence of upward swimming, it would take a larva on average 2.5 h to reach the bottom with $w_{sink} = 0.1$ mm s^{-1}. The same three patch radii as in the unsteady wind runs were chosen based on their passive tracer residence times from Fig. 17 relative to this average sinking timescale T_{sink}: r_{veg} = 0.5 m ($\lesssim T_{\text{sink}}$), r_{veg} = 3 m ($\gtrsim T_{\text{sink}}$), and r_{veg} = 8 m ($> T_{\text{sink}}$). No r_{veg} had a passive residence time approximately equal to 2.5 h, so the next closest r_{veg} values on either end were chosen. The simulations were run with the steady-state velocity fields from model runs with five patches of vegetation and a rightward wind (Runs 5, 8, and 13). For comparison with the

passive tracer particle cases, simulations were run without re-entrainment for up to three days or until less than 1% of the particles remained in the side pond. The fraction of particles remaining in the side pond over the course of the random walk simulations is plotted in Fig. 22 for each of the three r_{veg} values along with the comparable passive tracer cases from Fig. 15. The residence times, taken to be the time after which less than twenty percent of the initialized particles are remaining in the side pond, are given in Table 3. Residence times increase significantly with the inclusion of sinking. As particles sink deeper in the water column, they experience weaker velocities, slowing their eventual exit from the pond. $r_{veg} = 0.5$ m has the smallest increase in residence time, as about half of the particles exit the pond before sinking deep enough in the water column to experience a significant slowing of advective transport. Similarly, $r_{veg} = 8$ m has the largest increase in residence time, as less than 10% of the particles exit the pond before slowing. These increases in residence time would likely be less significant if vertical swimming was also incorporated, as particles would alternate between upward swimming and downward sinking, sampling both increased and decreased velocities and generally aggregating near the top of the water column. However, this analysis likely provides an upper bound on the effect of including particle sinking in the model on residence times.

Acknowledgements This work was supported by the US-National Science Foundation, Ecology and Evolution of Infectious Diseases program (grant number: DEB - 2011179).

Author contributions A.J.C., C.L.W., O.B.F., and G.A.D.L. conceptualized and designed research; B.J.P. performed research and prepared the main manuscript text; O.B.F. and G.A.D.L reviewed and edited the manuscript.

Data availability No datasets were generated or analysed during the current study.

Declarations

Conflict of interest The authors have no Conflict of interest to declare that are relevant to the content of this article. The authors declare no Conflict of interest.

References

1. WHO: Schistosomiasis (2016) number of people treated worldwide in 2014. Releve Epidemiologique Hebdomadaire 91(5), 53–60
2. WHO: Schistosomiasis Fact Sheet (2023). https://www.who.int/news-room/fact-sheets/detail/schistosomiasis
3. Sokolow SH, Huttinger E, Jouanard N, Hsieh MH, Lafferty KD, Kuris AM, Riveau G, Senghor S, Thiam C, N'Diaye A, Faye DS, De Leo GA (2015) Reduced transmission of human schistosomiasis after restoration of a native river prawn that preys on the snail intermediate host. Proc Natl Acad Sci 112(31):9650–9655. https://doi.org/10.1073/pnas.1502651112

4. Arostegui M, Wood C, Jones I, Chamberlin A, Jouanard N, Faye D, Kuris A, Riveau G, De Leo G, Sokolow S (2019) Potential biological control of schistosomiasis by fishes in the lower Senegal river basin. Am J Trop Med Hyg 100:117–126. https://doi.org/10.4269/ajtmh.18-0469
5. Hoover CM, Sokolow SH, Kemp J, Sanchirico JN, Lund AJ, Jones IJ, Higginson T, Riveau G, Savaya A, Coyle S, Wood CL, Micheli F, Casagrandi R, Mari L, Gatto M, Rinaldo A, Perez-Saez J, Rohr JR, Sagi A, Remais JV, De Leo GA (2019) Modelled effects of prawn aquaculture on poverty alleviation and schistosomiasis control. Nat Sustain 2(7):611–620. https://doi.org/10.1038/s41893-019-0301-7
6. Rohr JR, Sack A, Bakhoum S, Barrett CB, Lopez-Carr D, Chamberlin AJ, Civitello DJ, Diatta C, Doruska MJ, De Leo GA, Haggerty CJE, Jones IJ, Jouanard N, Lund AJ, Ly AT, Ndione RA, Remais JV, Riveau G, Schacht A-M, Seck M, Senghor S, Sokolow SH, Wolfe C (2023) A planetary health innovation for disease, food and water challenges in Africa. Nature 619(7971):782–787. https://doi.org/10.1038/s41586-023-06313-z
7. Krishnamurthy D, Katsikis G, Bhargava A, Prakash M (2017) *Schistosoma mansoni* cercariae swim efficiently by exploiting an elastohydrodynamic coupling. Nat Phys 13(3):266–271. https://doi.org/10.1038/nphys3924
8. Fingerut JT, Ann Zimmer C, Zimmer RK (2003) Larval swimming overpowers turbulent mixing and facilitates transmission of a marine parasite. Ecology 84(9):2502–2515. https://doi.org/10.1890/02-4035
9. Morley NJ (2012) Cercariae (Platyhelminthes: Trematoda) as neglected components of zooplankton communities in freshwater habitats. Hydrobiologia 691(1):7–19. https://doi.org/10.1007/s10750-012-1029-9
10. DiBenedetto MH, Koseff JR, Ouellette NT (2019) Orientation dynamics of nonspherical particles under surface gravity waves. Phys Rev Fluids 4(3):034301. https://doi.org/10.1103/PhysRevFluids.4.034301
11. Yang J, Francois N, Punzmann H, Shats M, Xia H (2019) Diffusion of ellipsoids in laboratory two-dimensional turbulent flow. Phys Fluids 31(8):085116. https://doi.org/10.1063/1.5113734
12. Zhang H, Ahmadi G, Fan F-G, McLaughlin JB (2001) Ellipsoidal particles transport and deposition in turbulent channel flows. Int J Multiph Flow 27(6):971–1009. https://doi.org/10.1016/S0301-9322(00)00064-1
13. Mortensen PH, Andersson HI, Gillissen JJJ, Boersma BJ (2008) Dynamics of prolate ellipsoidal particles in a turbulent channel flow. Phys Fluids 20(9):093302. https://doi.org/10.1063/1.2975209
14. Li R-Y, Cui Z-W, Huang W-X, Zhao L-H, Xu C-X (2019) On rotational dynamics of a finite-sized ellipsoidal particle in shear flows. Acta Mech 230(2):449–467. https://doi.org/10.1007/s00707-018-2295-z
15. Ciddio M, Mari L, Sokolow SH, De Leo GA, Casagrandi R, Gatto M (2017) The spatial spread of schistosomiasis: a multidimensional network model applied to Saint-Louis region, Senegal. Adv Water Resour 108:406–415. https://doi.org/10.1016/j.advwatres.2016.10.012
16. Perez-Saez J, Mande T, Larsen J, Ceperley N, Rinaldo A (2017) Classification and prediction of river network ephemerality and its relevance for waterborne disease epidemiology. Adv Water Resour 110:263–278. https://doi.org/10.1016/j.advwatres.2017.10.003
17. Perez-Saez J, Mande T, Rinaldo A (2019) Space and time predictions of schistosomiasis snail host population dynamics across hydrologic regimes in Burkina Faso. Geospatial Health. https://doi.org/10.4081/gh.2019.796
18. Mari L, Bertuzzo E, Finger F, Casagrandi R, Gatto M, Rinaldo A (2015) On the predictive ability of mechanistic models for the Haitian cholera epidemic. J Royal Soc Interface 12(104):20140840. https://doi.org/10.1098/rsif.2014.0840
19. Rinaldo A, Gatto M, Rodriguez-Iturbe I (2018) River networks as ecological corridors: A coherent ecohydrological perspective. Adv Water Resour 112:27–58. https://doi.org/10.1016/j.advwatres.2017.10.005
20. ...Wood CL, Sokolow SH, Jones IJ, Chamberlin AJ, Lafferty KD, Kuris AM, Jocque M, Hopkins S, Adams G, Buck JC, Lund AJ, Garcia-Vedrenne AE, Fiorenza E, Rohr JR, Allan F, Webster B, Rabone M, Webster JP, Bandagny L, Ndione R, Senghor S, Schacht A-M, Jouanard N, Riveau G, De Leo GA (2019) Precision mapping of snail habitat provides a powerful indicator of human schistosomiasis transmission. Proc Natl Acad Sci 116(46):23182–23191. https://doi.org/10.1073/pnas.1903698116
21. Sandoval J, Mignot E, Mao L, Pastén P, Bolster D, Escauriaza C (2019) Field and numerical investigation of transport mechanisms in a surface storage zone. J Geophys Res Earth Surf 124(4):938–959. https://doi.org/10.1029/2018JF004716

22. Rockwell D, Knisely C (1980) Observations of the three-dimensional nature of unstable flow past a cavity. Phys Fluids 23(3):425–431. https://doi.org/10.1063/1.863009
23. Jackson TR, Haggerty R, Apte SV, O'Connor BL (2013) A mean residence time relationship for lateral cavities in gravel-bed rivers and streams: incorporating streambed roughness and cavity shape. Water Resour Res 49(6):3642–3650. https://doi.org/10.1002/wrcr.20272
24. Chang K, Constantinescu G, Park S-O (2006) Analysis of the flow and mass transfer processes for the incompressible flow past an open cavity with a laminar and a fully turbulent incoming boundary layer. J Fluid Mech 561:113–145. https://doi.org/10.1017/S0022112006000735
25. Oliveira LED, Costa FR, Gualtieri C, Janzen JG (2022) Effects of vegetation density on sediment transport in lateral cavities. Environ Sci Proceed 21(1):16. https://doi.org/10.3390/environsciproc2022021016
26. Xiang K, Yang Z, Huai W, Ding R (2019) Large eddy simulation of turbulent flow structure in a rectangular embayment zone with different population densities of vegetation. Environ Sci Pollut Res 26(14):14583–14597. https://doi.org/10.1007/s11356-019-04709-x
27. Lu J, Dai HC (2016) Large eddy simulation of flow and mass exchange in an embayment with or without vegetation. Appl Math Model 40(17):7751–7767. https://doi.org/10.1016/j.apm.2016.03.026
28. Bye JAT (1966) Numerical solutions of the steady-state vorticity equation in rectangular basins. J Fluid Mech 26(3):577–598. https://doi.org/10.1017/S0022112066001411
29. Kumagai M (1982) A numerical study of wind-driven circulation in rectangular cavities. J Comput Phys 47(1):130–145. https://doi.org/10.1016/0021-9991(82)90068-7
30. Ulloa HN, Constantinescu G, Chang K, Horna-Munoz D, Hames O, Wüest A (2020) Horizontal transport under wind-induced resonance in stratified waterbodies. Phys Rev Fluids 5(5):054503. https://doi.org/10.1103/PhysRevFluids.5.054503
31. Fringer OB, Gerritsen M, Street RL (2006) An unstructured-grid, finite-volume, nonhydrostatic, parallel coastal ocean simulator. Ocean Model 14(3):139–173. https://doi.org/10.1016/j.ocemod.2006.03.006
32. Engwirda, D (2014) Locally optimal Delaunay-refinement and optimisation-based mesh generation. Ph.D., School of Mathematics and Statistics, The University of Sydney https://ses.library.usyd.edu.au/handle/2123/13148
33. McCoy A, Constantinescu G, Weber L (2008) Numerical investigation of flow hydrodynamics in a channel with a series of groynes. J Hydraul Eng. https://doi.org/10.1061/(ASCE)0733-9429(2008)134:2(157)
34. Zhang Y (2017) Numerical Modeling for Hydrodynamics and Suspended Sediment Transport in Estuarine Marshes. Ph.D. Dissertation, Stanford University, United States – California. https://www.proquest.com/docview/2508534394/abstract/6A10E2D617A14D20PQ/1
35. Plott JR, Diplas P, Kozarek J, Dancey CL, Hill C, Sotiropoulos F (2013) A generalized log law formulation for a wide range of boundary roughness typically encountered in natural streams. J Geophys Res Earth Surf 118(3):1419–1431. https://doi.org/10.1002/jgrf.20104
36. Jill S. Dodds (2022) Potamogeton zosteriformis Rare Plant Profile. New Jersey Department of Environmental Protection Office of Natural Lands Management New Jersey Natural Heritage Program. https://nj.gov/dep/parksandforests/natural/heritage/rareplantprofiles.html
37. Kantrud HA (1990) Sago pondweed (*Potamogeton pectinatus* L.): a literature review. Technical Report 176, U.S. Fish and Wildlife Service. https://pubs.usgs.gov/publication/2000134
38. Haggerty CJE, Bakhoum S, Civitello DJ, Leo GAD, Jouanard N, Ndione RA, Remais JV, Riveau G, Senghor S, Sokolow SH, Sow S, Wolfe C, Wood CL, Jones I, Chamberlin AJ, Rohr JR (2020) Aquatic macrophytes and macroinvertebrate predators affect densities of snail hosts and local production of schistosome cercariae that cause human schistosomiasis. PLOS Negl Trop Dis 14(7):0008417. https://doi.org/10.1371/journal.pntd.0008417
39. Nguyen KH, Gemmell BJ, Rohr JR (2020) Effects of temperature and viscosity on miracidial and cercarial movement of Schistosoma mansoni: ramifications for disease transmission. Int J Parasitol 50(2):153–159. https://doi.org/10.1016/j.ijpara.2019.12.003
40. Brown CA, Jackson GA, Brooks DA (2000) Particle transport through a narrow tidal inlet due to tidal forcing and implications for larval transport. J Geophys Res Oceans 105(C10):24141–24156. https://doi.org/10.1029/2000JC000211
41. Cerejo M, Dias JM (2007) Tidal transport and dispersal of marine toxic microalgae in a shallow, temperate coastal lagoon. Mar Environ Res 63(4):313–340. https://doi.org/10.1016/j.marenvres.2006.10.005
42. Sentchev A, Korotenko K (2004) Stratification and tidal current effects on larval transport in the eastern english channel: observations and 3D modeling. Environ Fluid Mech 4(3):305–331. https://doi.org/10.1023/B:EFMC.0000024246.39646.1d

43. Abdel Malek E (1958) Factors conditioning the habitat of bilharziasis intermediate hosts of the family Planorbidae. Bull World Health Organ 18(5–6):785–818
44. Fischer HB, List EJ, Koh RCY, Imberger J, Brooks NH (1979) Chapter 4 - Shear Flow Dispersion. In: Fischer HB, List EJ, Koh RCY, Imberger J, Brooks NH (eds) Mixing in Inland and Coastal Waters. Academic Press, San Diego, pp 80–103
45. Elder JW (1959) The dispersion of marked fluid in turbulent shear flow. J Fluid Mech 5(4):544–560. https://doi.org/10.1017/S0022112059000374
46. Holly FM, Usseglio-Polatera J-M (1984) Dispersion simulation in two-dimensional tidal flow. J Hydraul Eng 110(7):905–926. https://doi.org/10.1061/(ASCE)0733-9429(1984)110:7(905)
47. Murphy E, Ghisalberti M, Nepf H (2007) Model and laboratory study of dispersion in flows with submerged vegetation. Water Resour Res. https://doi.org/10.1029/2006WR005229
48. Huang L, Fang H, Reible D (2015) Mathematical model for interactions and transport of phosphorus and sediment in the Three Gorges Reservoir. Water Res 85:393–403. https://doi.org/10.1016/j.watres.2015.08.049
49. Stride B, Abolfathi S, Odara MGN, Bending GD, Pearson J (2023) Modeling microplastic and solute transport in vegetated flows. Water Resour Res 59(5):2023–034653. https://doi.org/10.1029/2023WR034653
50. Zeng Y, Huai W (2014) Estimation of longitudinal dispersion coefficient in rivers. J Hydro-Environ Res 8(1):2–8. https://doi.org/10.1016/j.jher.2013.02.005
51. Farzadkhoo M, Keshavarzi A, Hamidifar H, Javan M (2018) A comparative study of longitudinal dispersion models in rigid vegetated compound meandering channels. J f Environ Manag 217:78–89. https://doi.org/10.1016/j.jenvman.2018.03.084
52. Arya Azar N, Ghordoyee Milan S, Kayhomayoon Z (2021) The prediction of longitudinal dispersion coefficient in natural streams using LS-SVM and ANFIS optimized by Harris hawk optimization algorithm. J Contam Hydrol 240:103781. https://doi.org/10.1016/j.jconhyd.2021.103781
53. Ukpaka C, Agunwamba JC (2023) An improved equation development for longitudinal dispersion coefficient. Water Sci Technol 88(10):2521–2532. https://doi.org/10.2166/wst.2023.362
54. Ginetsinskaya TA (1988) Trematodes, Their Life Cycles. Biology and Evolution. Amerind Pub, New Delhi
55. Niang SAA, Drame MS, Gueye A, Sarr A, Toure MD, Diop D, Ndiaye SO, Talla K (2023) Temporal dynamics of energy production at the Taïba Ndiaye wind farm in Senegal. Discover Energy 3(1):6. https://doi.org/10.1007/s43937-023-00018-0
56. Jones IJ, Sokolow SH, Chamberlin AJ, Lund AJ, Jouanard N, Bandagny L, Ndione R, Senghor S, Schacht A-M, Riveau G, Hopkins SR, Rohr JR, Remais JV, Lafferty KD, Kuris AM, Wood CL, Leo GD (2021) Schistosome infection in Senegal is associated with different spatial extents of risk and ecological drivers for *Schistosoma haematobium* and S. *mansoni*. PLOS Neglected Tropical Diseases 15(9):0009712. https://doi.org/10.1371/journal.pntd.0009712
57. WHO: Field use of molluscicides in schistosomiasis control programmes: an operational manual for programme managers (2017). https://www.who.int/publications/i/item/9789241511995